RSC Advances

PAPER

View Article Online
View Journal | View Issue

Cite this: *RSC Adv.*, 2026, **16**, 23945

Evaluating the impact of CO_2 on the geomechanical and geochemical properties of different rock types

William Holdbrook Dontoh,[a] Mubarak M. Alhajeri,[b] Kim Mews,[a] Jyun Syung Tsau,[a] Robert Goldstein[c] and Reza Barati *[ac]

The interaction between CO_2 and water in subsurface environments plays a critical role in altering the geomechanical properties of rocks, with significant implications for carbon sequestration, reservoir integrity, and underground storage applications. This study evaluates the impact of CO_2-water exposure on the strength, elasticity, porosity, and mineralogical composition of different rock types, including sandstone, limestone, dolomite, basalt and shale. Laboratory experiments were conducted to characterize the initial petrophysical and geomechanical properties of the rock samples before subjecting them to CO_2-saturated water under controlled pressure and temperature conditions. Post-exposure analyses were performed using nanoindentation SEM-EDS and X-ray diffraction (XRD) to assess mineralogical and structural changes. The results indicate that CO_2-water interaction leads to varying degrees of mechanical weakening, with carbonate rocks showing significant dissolution effects and reduced elastic modulus. In contrast, silicate-rich rocks like sandstone exhibited comparatively lower degradation due to their mineralogical stability. These findings highlight the importance of rock-specific evaluations in subsurface engineering applications, particularly in optimizing CO_2 storage strategies and ensuring long-term stability. Further studies incorporating extended exposure durations and field-scale validation are recommended to enhance predictive models for rock behavior in CO_2-rich environments.

Received 6th January 2026
Accepted 20th April 2026

DOI: 10.1039/d6ra00145a

rsc.li/rsc-advances

Introduction

For carbon sequestration, enhanced oil recovery (EOR), geothermal systems, and natural CO_2 reservoirs, CO_2 interacts with the resident aqueous phase and the subsurface rocks. In carbon storage projects, supercritical CO_2 is injected into the subsurface, where it interacts with minerals and formation water to produce physicochemical reactions that change over time.[1] Likewise, supercritical CO_2 is injected into oil reservoirs during EOR operations, where it reacts with the surrounding rock matrix and reservoir fluids.[2] In geothermal systems, CO_2-bearing fluids circulate through fractured formations, creating complex interactions between gas, water, and minerals.[3]

CO_2 enhanced oil recovery

Enhanced Oil Recovery (EOR) is a method utilized to extract residual oil from reservoirs usually after primary and secondary recovery methods have been applied to produce the oil from porous rock.[4] EOR techniques can increase recovery factors to 30–60%, compared to 20–40% from primary and secondary methods.[5] By using these techniques, recovery rates are accelerated and residual oil in the matrix porosity is reduced.[4]

Carbon dioxide (CO_2) flooding is a proven EOR method that has been utilized for decades to increase oil production from mature reservoirs.[6] The process results in oil swelling, viscosity reduction, and miscible displacement, and under ideal circumstances, it can achieve a displacement efficiency as high as 100%. Water-rock interactions in CO_2-rich environments during EOR can greatly impact reservoir properties and oil recovery efficiency. Experimental studies have demonstrated that injecting CO_2-rich fluids into limestone and dolomite reservoirs causes mineral dissolution, especially of calcite, leading to increased porosity and permeability.[7,8] Water salinity, pressure, displacement type, and injection rate, affect how severe these reactions are.[9] The interactions have the potential to enhance oil recovery and CO_2 storage capacity, but they may also compromise the integrity of the reservoir's seal. While high Ca^{2+} concentrations in formation water can prevent calcite dissolution, higher CO_2 partial pressures accelerate the dissolution of minerals like feldspar and carbonate cements.[8] These complex CO_2-brine-rock interactions are crucial for optimization of CO_2 sequestration and EOR processes.[10]

[a]*Tertiary Oil Recovery Program (TORP), University of Kansas, Department of Chemical & Petroleum Eng, Lawrence, Kansas, USA. E-mail: rbarati@gmail.com*

[b]*The Public Authority for Applied Education and Training (PAAET), Kuwait*

[c]*Kansas Interdisciplinary Consortium for Earth, Energy and Environment (KICE[3]), University of Kansas, Department of Geology, Lawrence, Kansas, USA*

Geological carbon storage

Carbon Capture and Storage (CCS) is a technology designed to reduce CO_2 emissions from energy-related and industrial sources in order to mitigate global warming.[11] In this procedure, CO_2 is captured, transported, and stored away.[12] Storage in geological storage saline aquifer reservoirs and basalts are among the main storage techniques.[13,14] Like EOR procedures, carbon capture and storage (CCS) projects depend heavily on CO_2-water-rock interactions, which have an impact on reservoir characteristics, precipitation, and mineral dissolution. Higher subsurface temperature accelerates the corrosion of feldspars, silica, and clay minerals, according to experimental research.[15] These interactions can lead to changes in porosity and permeability, potentially enhancing CO_2 injectivity in low-permeability formations.[16] Transport processes often inhibit the dissolution of fast-reacting minerals, including carbonates, but slower-reacting minerals may remain out of equilibrium for prolonged periods of time.[17] Temperature, pressure, and brine salinity are some of the variables that affect reaction rates.[16]

Rock types in CO_2-Brine interactions for subsurface storage and EOR

In geological and technical applications, basalt, limestone, dolomite, sandstone, and shale are some of the most researched rock types due to their properties as storage sinks, EOR candidates or caprocks. Samples from various rock types are highlighted in this study in order to evaluate their mechanical behavior following exposure to CO_2-brine.

Firstly, basalt is a fine-grained mafic igneous rock that is mostly made up of olivine, pyroxene, and plagioclase. It is a stable option for subsurface applications because of its high strength, porosity, and capability of mineralizing the CO_2.[3] Three examples of basalts used in this study are Kilbourne Hole and the Carrizozo Lava Flow, both from New Mexico, and basalt from the Fagradalsfjall, Iceland 2021 eruption. These basalts were chosen because they were relatively young and had little weathering alteration. Kilbourne Hole is a well-known example of a maar volcano created by phreatomagmatic explosions, in the southern New Mexico Potrillo volcanic field. Carrizozo Lava Flow is a more recent and effusive basaltic event which is situated in the Tularosa Basin of New Mexico, northeast of Kilbourne Hole. It originated from Little Black Peak some 5000 years ago.[18] The Carrizozo Basalt, which was formed by partial melting of a spinel lherzolite mantle source and shows slight crystal fractionation, is chemically slightly alkaline to intermediate olivine basalt, and again, it is part of the Rio Grande Rift system. The youngest sample comes from the Fagradalsfjall 2021 eruption on Iceland's Reykjanes Penninsula, which resulted from the coinciding mid-Atlantic ridge and Icelandic plume.[19] These basalts are highly vesicular, consisting of plagioclase, olivine, clinopyroxene, and Cr-Spinel in a glassy matrix.[20] These samples were collected only two years after the eruption and are essentially unaltered by weathering processes. Limestone, a sedimentary rock mostly consisting of calcite ($CaCO_3$), is widely distributed in carbonate reservoir rocks and has high reactivity in fluid–rock interactions, with large porosity changes caused by diagenetic processes.[21] The limestone used in the study is the Mississippian Salem Limestone of Indiana. Dolomites, like limestones, are carbonate rocks, but made primarily of the mineral dolomite ($CaMg(CO_3)_2$), which is formed through diagenetic modification of limestone by magnesium-rich fluids. This process, known as dolomitization, commonly happens in shallow marine areas under evaporitic circumstances.[22] Dolomites are important in both academic and industrial contexts because of their capacity to maintain porosity and permeability, making them valuable hydrocarbon reservoirs. The dolomite sample used in this study is of Silurian age. Sandstone, another typical sedimentary rock, is composed of detrital sand-sized particles of predominantly of quartz and feldspar, with its porosity and permeability largely determined by the degree of cementation and grain sorting.[23] The sample of sandstone used is Pennsylvanian in age Bandera Sandstone, from Kansas. Shale or mudrock is a fine-grained, clay- and silt-rich sedimentary rock known for its low permeability and high organic content, making it significant in unconventional hydrocarbon reservoirs and seals for CO_2 storage.[24] The shale sample we use is Devonian in age, Woodford Shale, from Oklahoma.

Effects of CO_2 on various rock types

The interaction of the rock types proposed with CO_2-saturated water is hypothesized to differ greatly due to changes in mineralogy and porosity. When exposed to CO_2-water systems, basalt, which contains reactive silicate mineral or glass, can induce carbonate mineral precipitation, potentially improving mechanical stability over time.[25] In contrast, when limestone comes into contact with fluids that are rich in CO_2, it experiences dissolution–precipitation reactions that alter its porosity and may have an effect on its geomechanical characteristics. Limestone is extremely soluble in acidic environments.[26] Sandstone's response to CO_2 exposure depends on its cementing materials; quartz-cemented sandstones exhibit minimal changes, whereas carbonate-cemented varieties are prone to dissolution and strength reduction.[27] Shale or mudrock reactions depend on mineralogy. For example, high clay mineral content can cause mineral alterations and swelling when the clays interact with water that has been acidified by CO_2, which could lessen the rock's ability to seal as a caprock for CO_2 storage.[28] Several studies have used field research, laboratory experiments, and numerical modelling to examine the geochemical and geomechanical impacts of CO_2-rock interactions. Increased porosity damaged the rock structure, according to Noiriel *et al.*'s analysis of the dissolution of carbonate rocks in CO_2-rich environments. However, their research was restricted to short-term interactions and failed to account for long-term diagenetic impacts.[21] High-pressure tests were carried out by Kaszuba *et al.* on Silurian Maplewood shale and Arkose as mineralogical and geochemical representations of aquitard and aquifer, respectively. Equal proportions of quartz, oligoclase, and microcline made up the majority of the arkose. On the other hand, the shale was rich in quartz and clay minerals. Although the trials showed mineral breakdown and

subsequent precipitation and replicated deep CO_2 sequestration, they lacked comprehensive mechanical testing to measure strength degradation.[27] Espinoza & Santamarina, in their investigation of the effects of CO_2-brine on caprock integrity, also demonstrated that shales may undergo swelling and a decrease in strength; nevertheless, their main focus was on permeability alterations rather than direct mechanical weakening.[29] Zhao *et al.* further investigated the changes caused by CO_2 in sandstones, focusing on the evolution of porosity, although they did not examine elastic properties such as Young's modulus after the response.[30] Although these investigations provide important insights into the mineralogical alterations imposed by CO_2, mechanical testing is required to more accurately evaluate structural integrity. This work examines how short-term alteration in CO_2-rich solutions affects the grain-scale geomechanics in various rocks.

Rock geomechanics and nanoindentation

Geomechanics is a significant aspect of dealing with the subsurface, especially in regions where integrity is critical. In areas such as petroleum, accurate information about how formations respond to stresses during fracturing, drilling, and well completion is required. Rock Mechanics is also critical in carbon utilization and sequestration as both bulk and surface properties.

Nanoindentation is an effective technique for assessing mechanical properties of rocks particularly at the microscale. Oliver and Pharr created the fundamental nanoindentation method to evaluate hardness and Young's modulus using load-displacement curves, providing a higher-resolution alternative to existing methods.[31] Bobko and Ulm used nanoindentation to differentiate between cemented and uncemented phases in sedimentary rocks. This is especially important in CO_2-exposed formations where dissolution happens at the microstructural level.[32] Conventional mechanical testing methods, like uniaxial/triaxial compression and ultrasonic velocity measurements, have limits for evaluating small scale samples. These methods also do not describe the micro-scale changes occurring at the pore surface. Uniaxial compressive strength (UCS) tests provide bulk mechanical parameters, but are damaging, require large samples, and fail to measure microscale alterations.[33] Ultrasonic velocity measurements, which are commonly used to evaluate elastic characteristics, presuppose uniformity and can be insensitive to localized mineral dissolution or microcrack formation.[34] Mews (2020) carried out a multi-scale geomechanical comparison for unconventional reservoirs, demonstrating the utility of Atomic Force Microscopy (AFM) PeakForce Quantitative Nanomechanical Mapping (PF-QNM) in characterising rock attributes at the microscale. The study presented an iterative correction approach for Young's modulus based on Poisson's ratio, which increased the technique's accuracy. One significant advantage identified was AFM PF-QNM's capacity to analyze relatively small samples, such as drill cuttings, allowing for the measurement of 3D heterogeneity in reservoir rocks.[35] The ability of nanoindentation to identify mechanical heterogeneity at the grain scale allows for a more thorough evaluation of the ways in which CO_2-induced changes impact rock stiffness at various stages.[36] The small penetration depths of nanoindentation, which might not adequately capture bulk mechanical properties, the inability to measure the elastic properties of the frame and the difficulties in analyzing highly porous or heterogeneous samples are some of its drawbacks.[37]

Mineral composition, porosity, cementation, fluid saturation, and diagenetic changes are some of the extrinsic and intrinsic elements that affect the elastic properties of rocks, especially Young's modulus. The stiffness of rocks is largely determined by their mineral composition; for instance, rocks that are rich in quartz typically have higher Young's modulus values, while rocks that are rich in clay and carbonate typically have lower stiffness.[38] Porosity and permeability also have a big impact on elastic characteristics because more porosity reduces the amount of contact between load-bearing grains, which makes the rock less rigid overall.[39] The extent of cementation affects grain interactions under stress, with well-cemented rocks demonstrating greater modulus values than poorly cemented formations.[40] The presence of fluids modifies elastic characteristics by influencing grain contacts, increasing pore pressure, and reducing effective stress, resulting in a decrease in Young's modulus.[41] The Young's modulus of limestone samples from Gua Kandu and Rapat in Ipoh, Perak, was reported by Serasa *et al.*,[42] and the results show variation in measurements and techniques. Results from static and dynamic measurements frequently differ, with dynamic methods usually overestimating values.

The mechanical characteristics of limestone are influenced by moisture content and bedding orientation. In limestone, water saturation can lower the shear and Young's moduli.[43] A new method for determining the modulus of elasticity was proposed, showing comparable results to stress–strain curve measurements.[44] These results demonstrate how difficult it is to determine limestone's Young's modulus precisely and how crucial it is to take a variety of parameters into account while doing measurements. Young's modulus can be considerably affected by CO_2-water interaction with rocks through mechanical weakening, precipitation, and mineral dissolution. Young's modulus is lowered in carbonate rocks like limestone because CO_2-water acidifies the pore fluid and promotes calcite dissolution, which increases porosity and decreases load-bearing mineral connections.[21] Research has also shown that exposure to CO_2 significantly reduces the mechanical characteristics of rocks, with limestone rocks exhibiting a 95% reduction in Young's modulus.[45] In sandstone, the impact of CO_2-water exposure is highly dependent on the cementing material; carbonate-cemented sandstones undergo dissolution-induced weakening, while quartz-cemented sandstones often see negligible changes in Young's modulus.[27] Additionally, the degree of elastic property deterioration depends on the original porosity of the sandstone; higher porosity sandstones show larger losses because of increased CO_2-water penetration.[46]

In shale formations, Young's modulus can be affected by changes in mineralogy and microstructure brought about by CO_2-water interaction. Reactive clay minerals found in shales

can absorb CO_2-rich fluids, causing swelling, softening, and mechanical weakness.[28] This process reduces the rock's elastic stiffness and could lead to a loss of caprock integrity in reservoirs used to store CO_2. Further, depending on their clay content and exposure settings, CO_2-exposed shales may have a 15–40% decrease in Young's modulus, according to experimental research.[47] Basalts, on the other hand, are reported to demonstrate less susceptible to dissolution-driven weakening because of their silicate mineral composition, but CO_2-water interactions can induce mineral precipitation that may alter pore connectivity and slightly reduce elasticity over time.[3] However, the effect on Young's modulus in basalts is typically less pronounced than in sedimentary rocks. These results demonstrate that the degree of CO_2-induced degradation of elastic properties differs depending on the type of rock, with carbonate rocks showing the greatest reductions because of dissolution, shales changing because of clay-fluid interactions, and sandstones responding differently depending on their cementation and porosity. Predicting rock behavior in CO_2 sequestration projects and evaluating long-term pore-to-core stability requires an understanding of these processes.

Materials and methods

The properties of the different rock types were characterized to provide information about the nature of the rocks and how these factors would affect alteration in CO_2-rich water. Before exposing the rock samples to CO_2-saturated water, it was important to characterize their porosity, permeability, and mineral composition to establish a baseline for understanding the mechanical and chemical alterations that occur after exposure. For context, before exposure, the surfaces of the samples were polished and coated with gold for scanning electron microscopy (SEM). Afterwards, the surface is gently cleaned with a Kim wipe to remove the gold particles and nanoindentation is performed, followed by CO_2 water interaction. After exposure, the surface is again coated for SEM and then cleaned as well for nanoindentation.

Sample selection and preparation

Different rock samples were selected based on their mineralogical composition and relevance to geological storage and reservoir engineering. The types of rocks analyzed include Silurian dolomite, Bandera Gray sandstone, Woodford shale, Indiana limestone and basalts from New Mexico and Iceland. One inch core plugs and 7 × 7 × 3 mm size samples were made for every rock type as shown in Fig. 1. The samples were then dried to eliminate moisture within the pores. The surfaces of the cut size samples were polished to a rough surface of about 300 nm.

Experimental procedures

Steady state-air permeability. The core plugs were dried at 80 °C for 24 hours to ensure they were as dry as possible. This was to remove possible moisture from the pores to allow helium gas to flow through for accurate estimate of the porosity and

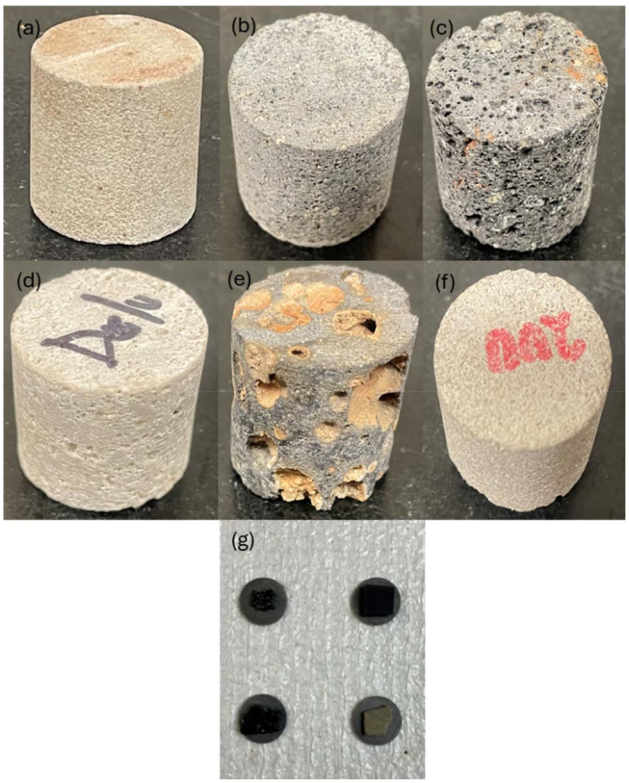

Fig. 1 Core plugs (1 inch length and diameter) and cut size samples (7 × 7 × 3 mm). (a) Bandera Gray sandstone (1 inch length and diameter), (b) Kilbourne Basalt A (1 inch length and diameter), (c) Carrizozo Basalt (1 inch length and diameter), (d) Silurian dolomite (1 inch length and diameter), (e) Kilbourne Basalt B (1 inch length and diameter), (f) Indiana limestone (1 inch length and diameter), (g) cut size samples (7 × 7 × 3 mm).

permeability. The core plugs were inserted into a core holder with confined and axial pressures of 350 psi and 100 psi, respectively. The confinement pressure helps to keep the core tightly held within the core holder to prevent the leakage of the gas. A flowmeter was connected to the outlet to measure the flowrates as shown in Fig. 2. Helium was pumped through the core at three different pressures and the corresponding flowrates measured. A plot of pressure *versus* flowrate and using the darcy equation, the permeability was calculated as:

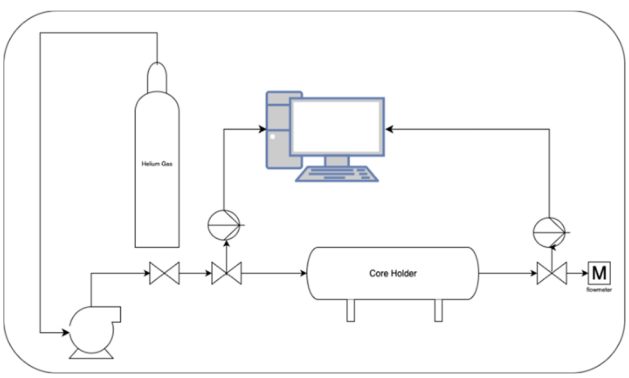

Fig. 2 Schematic of pulse decay experimental set up.

$$k = \frac{(2\mu L P_{SC}) T Q_{SC}}{A T_{SC}\left(P_2^2 - P_1^2\right)}$$

$$b = \frac{Q_{SC}}{\left(P_2^2 - P_1^2\right)}$$

$$k = \frac{(2\mu b L P_{SC}) T}{A T_{SC}}$$

where: b = the slope of the line from flowrate *vs.* difference between the squares of the pressures k = permeability, mD μ = dynamic viscosity of the gas at the operating temperature and pressure, cp L = length of core, cm A = area of core, cm^2 T_{SC} = temperature at standard conditions, K T = temperature, K Q_{SC} = flowrate of gas at standard conditions, cm^3 s^{-1} P_1 = downstream pressure, atm P_2 = upstream pressure, atm.

Pulse decay-air porosity. Using the same set up for steady state permeability but without the flowmeter, a pressure was set between 90 and 100 psi at the upstream against 0 psi at the downstream and allowed to decay within the core holder until an equilibrium pressure is achieved. The pressure drops were recorded and plotted against time. This method was used for tight rocks for which the steady state method does not apply.

Water porosity. The core samples were weighed dry and then saturated with water in a desiccator after pumping to vacuum to remove air trapped in the pores of the samples. After samples were well saturated, the samples were weighed again to determine the mass difference from which the porosity was calculated.

NMR porosity. The core samples were saturated with RO water for about 3 days and then weighed to determine the wet weight. The samples were then wrapped in a paraffin film to prevent the water from escaping from the pores after saturation. Each samples was held in the tube within an NMR Rock core analyzer and the T2 relaxation data was generated. Before this, the T2 relaxation data was generated for a standard RO water sample which was then used as a calibration sample for determining the porosities of the samples.

X-ray diffraction. End pieces of the cores were ground into powder and then transferred onto a sample holder which was inserted into the X-ray diffraction (XRD) equipment. Systematic errors in the preparation of the samples are a major source of analytical error and so care was taken in the sample preparation. XRD was used to determine the mineralogical composition of the rock samples, providing insights into their crystalline structures and phase distributions. The analysis was conducted using a Bruker D2 Phaser Powder Diffractometer with Cu-Kα radiation (λ = 1.5406 Å) at an operating voltage of 40 kV and a current of 40 mA. Samples were finely ground to a particle size of <75 μm to ensure homogeneity and reduce preferred orientation effects, which can influence peak intensities. Diffraction patterns were collected over a 2θ range of 5° to 80° at a step size of 0.03° with a dwell time of 1 second per step. The XRD data obtained were analyzed using the JADE software.

Scanning electron microscopy energy dispersive X-ray spectroscopy. The Hitachi S-4700 type II field emission scanning electron microscope at the Microscopy and Analytical Imaging Lab at KU was used to examine the materials' surface morphology and elemental composition. To improve electrical conductivity and improve image quality, a thin layer of gold was applied to the samples using a sputter coater prior to imaging. This was to reduce the excessive charging effect of the rock surface. To facilitate the relocation of spots with their associated coordinates prior to and during the CO_2 reaction, the surfaces of the samples were marked. In order to maximize resolution and elemental detection, SEM-EDS analysis was carried out under high vacuum circumstances using a condenser lens of 5, an accelerating voltage of 10 kV, an emission current of 8–10 μA, and a working distance of 12 mm.

Geomechanical testing-nanoindentation. The surfaces of the 7 × 7 × 3 mm samples were well polished to ensure uniformity across the surface and to eliminate inconsistencies between the contact area and the indenter tip. Using a loading/unloading force of 5000 μN and a holding time of 12 seconds, four precise locations were selected on the samples' surface. To calculate the Young's modulus and hardness of each sample, load displacement curves were generated using the Bruker Hysitron Nano indenter from KU's Bioengineering Lab. Nanoindentation was performed before and after exposure to CO_2.

CO_2-water exposure. After SEM and nanoindenting, the cut size samples were subjected to CO_2-saturated water under controlled conditions of 40 °C and 1200 psi to simulate typical Kansas reservoirs and keep the CO_2 in the supercritical state as shown in Fig. 3. The exposure was done for 5 days for each sample. A first Indiana limestone was ran alone and the other samples were paired during the run in this order; Sandstone and shale, Kilbourne A and B, Carrizozo and Iceland Basalts, dolomite and limestone. Samples were tested to determine whether their geomechanical and geochemical characteristics had changed after exposure. An Indiana limestone sample was used as a test to estimate the time after which the decline in the Young's modulus reached an equilibrium. Between the 96th and 120th hours, the Young's modulus stabilized and this provided a baseline for the exposure time for all the other samples since limestone was projected to be the most susceptible rock to CO_2

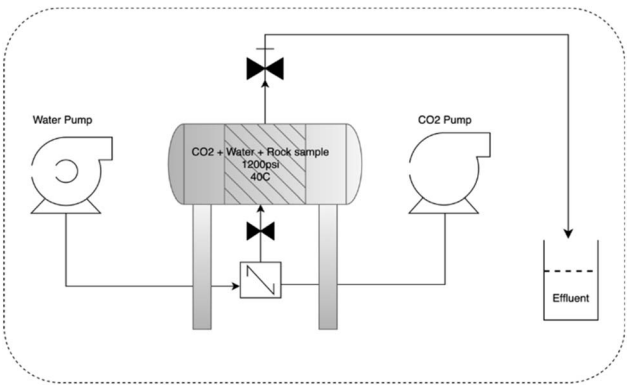

Fig. 3 Schematic for CO_2 rock interaction set up.

water. The ICP-OES measurements were used to analyze the ions present in the effluents from these reactions.

Results

Porosity and permeability for samples

Porosity and permeability play an important role in determining how CO_2-water infiltrates the rock, influencing the extent of mineral dissolution or precipitation, which can subsequently impact mechanical properties such as Young's modulus. Rocks with higher porosity and permeability may undergo more extensive fluid–rock interactions, causing greater structural weakening, while low-permeability rocks may show limited changes. As shown in Table 1, the rocks studied show a range of porosity and permeability data. Porosity and permeability were not tested for Iceland Basalt and Woodford Shale because their samples were too small to create core samples. Despite having intermediate porosity levels (~12–17%), Indiana limestone and Carrizozo Basalt had the highest air permeability values (121.34 mD and 86.78 mD, respectively) among the samples. Kilbourne Basalt A, on the other hand, showed a very low permeability (0.18 mD), indicating poorly connected or isolated pore spaces, even though it had detectable porosity (8.63%). The notable differences between Kilbourne Basalt A and B, with Kilbourne B exhibiting both increased porosity and somewhat improved permeability (4.73 mD), highlighting the underlying heterogeneity within basaltic rocks. Air and NMR porosity values were often highly correlated across samples, with air porosity commonly somewhat higher, perhaps because of variations in micropore and bound water sensitivity. The moderate porosity (10–15%) and permeability (4–26 mD) of the sandstone and dolomite samples were in line with their sedimentary origins and intergranular pore patterns. Overall, these patterns show that whereas porosity serves as a gauge for fluid storage capacity, permeability and fluid transport behavior are determined by the connection of these pore spaces, which is influenced by mineralogy and rock structure.

Mineral composition for samples

X-ray diffraction (XRD) analysis before interaction with CO_2 revealed a wide variety of mineral components in the various basalt samples. Labradorite (84.2%) made up the majority of the Carrizozo Basalt, with minor levels of quartz (8.6%) and diopside (7.3%), indicating a plagioclase-rich composition. Iceland Basalt, on the other hand, had a stronger mafic composition with a smaller percentage of labradorite (53.3%) but greater percentages of augite (28%), aegirine-augite (13.5%), and magnetite (5.2%). Although Kilbourne Basalt A contains langbeinite (5.7%), a potassium-magnesium sulfate mineral, likely a weathering product in New Mexico's arid environment, both Basalt A and B had high labradorite and augite contents. Kilbourne Basalt B differed compositionally from the other basalt samples due to its higher augite content (45.2%). The Silurian Dolomite was composed entirely of dolomite (100%), as would be expected for a well-preserved dolostone deposit. Similar to this, Indiana limestone, which is made entirely of calcite, is a common carbonate rock that dissolves easily in acidic CO_2-saturated liquids, which can drastically change its strength and permeability. The Bandera Gray sandstone was a quartz-dominated feldspathic sandstone, consisting of quartz (84.5%) and albite (15.5%). The mineral composition of the Woodford Shale was complex, with muscovite (40.1%), quartz (34%), zinnwaldite (15.6%), dolomite (8.9%), and scorodite (1.4%). The high proportion of muscovite and zinnwaldite (a lithium-rich mica) indicates a mica-rich shale, which can have a substantial impact on mechanical behavior and fluid interactions. These mineralogical differences show how various rock types may react differently to fluid interactions, mechanical stress, and exposure to CO_2-water.

Overall, shales featured a variety of clay-rich and mica-bearing assemblages, sandstones showed quartz-dominance with feldspathic influence, carbonates revealed pure compositions prone to dissolution, and basaltic rocks displayed a variety of mafic and felsic minerals. Under geological settings, these variations are critical in determining the evolution of porosity, changes in permeability, and mechanical stability. The measured characteristics of each of the eight samples are summarized in Table 1.

Additionally, establishing these characteristics prior to exposure guarantees experimental consistency, allowing for a fair comparison between various rock types and confirming that any mechanical changes seen are caused by CO_2-water interactions rather than intrinsic sample variability.

Table 1 Petrophysical properties of various rocks

Sample	Mineral composition	Air porosity, %	NMR porosity, %	Air permeability, mD
Carrizozo Basalt	Labradorite (84.2%), diopside (7.3%), quartz (8.6%)	16.79	15.33	86.78
Iceland Basalt	Labradorite (53.3%), augite (28%), aegirine-augite (13.5%), magnetite (5.2%)	—	—	—
Kilbourne Basalt A	Labradorite (58.7%), augite (35.6%), langbeinite (5.7%)	8.63	9.2	0.18
Kilbourne Basalt B	Labradorite (50.0%), augite (45.2%), trace minerals	18.85	16.0	4.73
Silurian dolomite	Dolomite (100%)	10.69	11.2	4.25
Bandera Gray sandstone	Quartz (84.5%), albite low (15.5%)	15.12	14.4	26.44
Woodford shale	Muscovite (40.1%), quartz (34%), zinnwaldite (15.6%), dolomite (8.9%), scorodite (1.4%)	—	—	—
Indiana limestone	Calcite (100%)	12.07	13.2	121.34

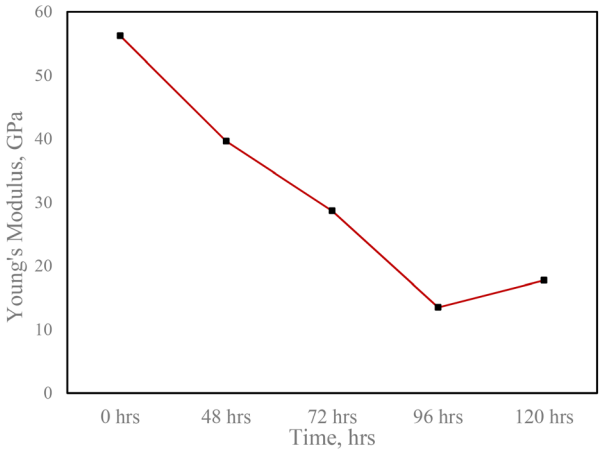

Fig. 4 Graph of Young's modulus *vs.* time for limestone sample.

Effect of CO_2 on Young's modulus of Indiana limestone

The nanoindentation results showed that the elasticity of the rocks, as evaluated by Young's modulus, declined during CO_2-water exposure. The Young's modulus for the Indiana limestone test sample decreased gradually from the first 24 hours until 120 hours, when it stabilized, as shown in Fig. 4. This indicates a progressive reaction depending on the rock type. To validate this, the sample's surface was re-polished after CO_2-water exposure to reveal a new surface, and the Young's modulus was measured to see whether the change in modulus occurred solely on the surface or throughout the bulk. The surface had a modulus of 55.9 GPa compared to 56 GPa before interaction with CO_2 rich water.

Comparison of geomechanical changes across rock types

According to a comparative examination, all rocks saw a decrease in Young's modulus, but the degree of the reduction differed based on the pore structure, carbonate content, and presence of reactive minerals. Table 2 summarizes each rock type's results. The Young's modulus measurements before and after CO_2 exposure show that the various rock types have distinct levels of mechanical weakening. In general, quartz-rich sandstones remained quite stable, while carbonate-rich rocks showed the greatest loss in stiffness. Shales and basalts had moderate to severe decreases, with differences related to their unique porosity and mineral assemblages.

Table 3 Ion concentrations in RO water

	Concentration of ions present in RO water before interaction, ppm			
Effluent	Ca^{2+}	Na^{+}	Al^{3+}	Mg^{2+}
Limestone	0.00	0.20	0.00	0.00
Sandstone & shale	0.00	0.20	0.00	0.00
Kilbourne A & B	0.00	0.20	0.00	0.00

Table 4 Ion concentration of effluent from rock and CO_2-rich water interaction

	Concentration of ions present in CO2-RO water after interaction, ppm			
Effluent	Ca^{2+}	Na^{+}	Al^{3+}	Mg^{2+}
Limestone	116.82	15.47	0.03	3.42
Sandstone & shale	43.37	11.11	0.21	7.46
Kilbourne A & B	75.35	4.40	0.03	3.27

Analysis of effluent water from interaction

ICP-OES was used to evaluate the effluent water from the interactions and determine which ions were dissolved. Ca^{2+}, Na^{+}, Al^{3+}, and Mg^{2+} were among the ions used as targets. As mentioned, the effluents collected were for paired samples with only Limestone reacted alone. Sandstone was paired with shale whereas Kilbourne A and B were also paired. The effluents for dolomite, Carizozo Basalt and Iceland Basalt were not collected due to leakage in the effluent collection line. The reactions were static reactions with no mixing and the volume of water in the cell was 11.56 mL. Table 3 shows the ionic concentrations of fresh RO water prior to interaction, which serves as a baseline for any rise in concentrations following interaction with the rock components. Table 4 summarizes the amounts of these ions in effluent water after CO_2-RO water-rock reaction. The results revealed that there were substantial ion concentrations in the effluents. Limestone effluent water had the highest Ca^{2+} content of 116.82 ppm. Na^{+} and Mg^{2+} were also present, albeit in lower amounts. Fig. 5 and 6 shows that the effluent from Woodford shale and sandstone had moderate quantities of Ca^{2+}, Na^{+}, and Mg^{2+}(43.37 ppm, 11.11 ppm and 7.46 ppm

Table 2 Changes in Young's modulus before and after CO_2 interaction for 120 hours

Samples	Average Young's Mod. Before CO_2 exposure, GPa	Average Young's Mod. After CO_2 exposure, GPa
Carrizozo-Basalt	118.63	84.95
Iceland Basalt	105.99	53.38
Kilbourne Basalt A	32.79	10.71
Kilbourne Basalt B	69.46	49.66
Silurian dolomite	148.38	104.79
Bandera Gray sandstone	21.65	20.08
Woodford shale	6.08	3.59
Indiana limestone	59.45	6.00

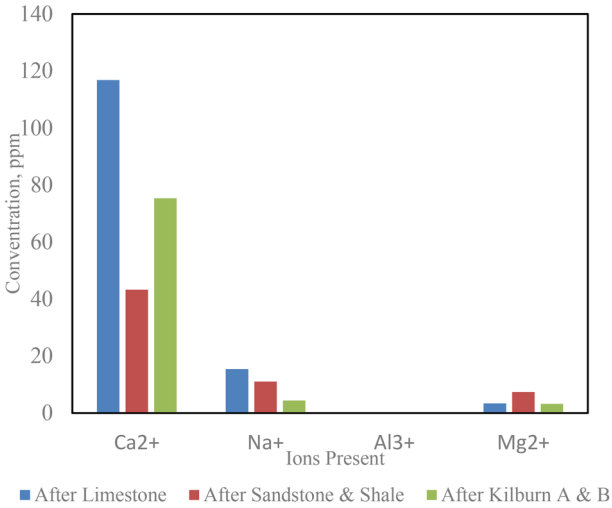

Fig. 5 Graph of ions present *versus* concentration in effluents after interactions.

respectively). Effluents from the Kilbourne A and B reactions likewise revealed the release of a high concentration of Ca^{2+}.

Surface analysis from SEM-EDS. SEM-EDS analysis was carried out on 8 samples to evaluate changes in microstructure and elemental composition after interaction with CO_2-rich water. This method allowed for a qualitative and semi-quantitative assessment of mineral surface changes, dissolving characteristics, and the redistribution or loss of critical components as a result of carbonic acid-driven processes. To provide a reference baseline, rock samples were initially described in their untreated state using SEM and analyzed by EDS. They were subsequently mechanically cleaned of gold coating and reacted with CO_2-rich water. Surface images were then acquired using SEM and EDS

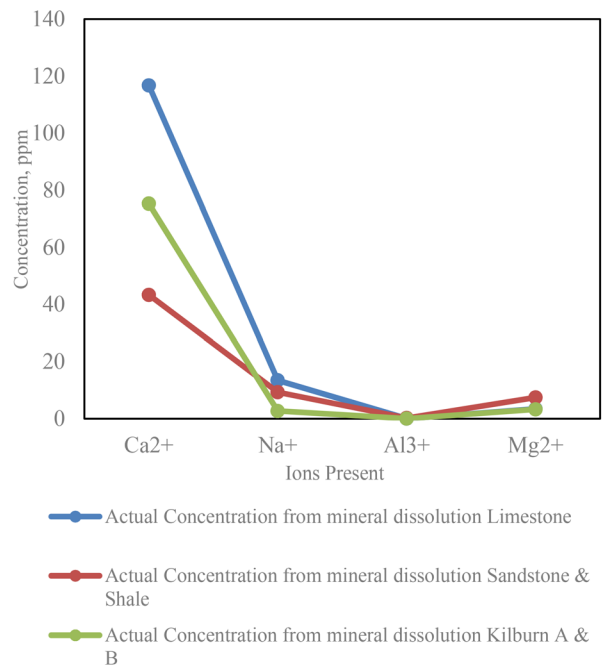

Fig. 6 Actual concentrations of ions dissolved in effluents.

was used to map elemental composition. This enabled direct comparisons between surface textures and chemical compositions before and after interaction.

Limestone showed the most significant alteration among all the samples. Its pre-exposure surface was reasonably smooth, but exposure caused the formation of new micropores, crystal edge disintegration, and increased surface roughness, as seen in Fig. 7. These visual alterations were accompanied by a significant retention of calcium content due to its pure calcitic nature across all four examined sites. Observed changes are consistent with the dissolution of calcite, the major constituent of the limestone. Trace increases in silicon and aluminum in some areas may indicate surface contamination, secondary mineral production, or the emergence of previously buried silicate phases (Fig. 7).

In contrast, the Woodford Shale showed no visible or chemical change. Prior to exposure, SEM images revealed the compacted, mineral alignment typical of fissile fine-grained clay-dominated rocks. Minor surface etching and delamination was seen following exposure, but porosity and cracking did not increase significantly as seen in Fig. 9. EDS examination revealed increases in aluminum, iron and a modest increase in surface carbon signal modulus.

Bandera sandstone provided an intermediate response. Initial SEM images in Fig. 10(a) revealed angular quartz grains with loosely packed intergranular gaps. Post-exposure photos revealed almost no observable changes with only minor surface infilling, as seen in Fig. 10(c). Silicon remained fairly steady, as expected from quartz, whereas minor increases in calcium and iron could indicate the formation of carbonate or iron oxide phases.

After exposure to CO_2-rich water, dolomite surfaces exhibited significant etching and small dissolution pits, despite being initially flat and polished. There was an unusual observation of what appeared to be a compositional change in the dolomite. Whiter areas in the SEM images showed more etching than darker areas, as seen in Fig. 8(c). Some film-like coatings were observed on the surface; however, these were most likely due to contamination. There was also an increase in silica and iron in some locations, but not elsewhere.

The four basalt samples exhibited varying responses, showing mineralogical variety among them. All four basalts most likely had an amorphous glass component, with Iceland basalt having the most. Iceland Basalt showed minimal etching. The darker patches, which are most likely plagioclase feldspar phases, appeared more etched, as illustrated in Fig. 11. The surface alterations in Carrizozo Basalt were identical to those seen in Fig. 12. Kilbourne A and B did not exhibit significant surface alterations but saw slight etching on their surfaces, as seen in Fig. 13 and 14. Ca, Fe, Al, and Si were released, however EDS analysis revealed a loss of Mg and Na (Table 5).

Discussion

Weakening after CO_2-Water reaction

The mechanical and microstructural responses of the studied rocks following CO_2-water exposure reveal a consistent pattern

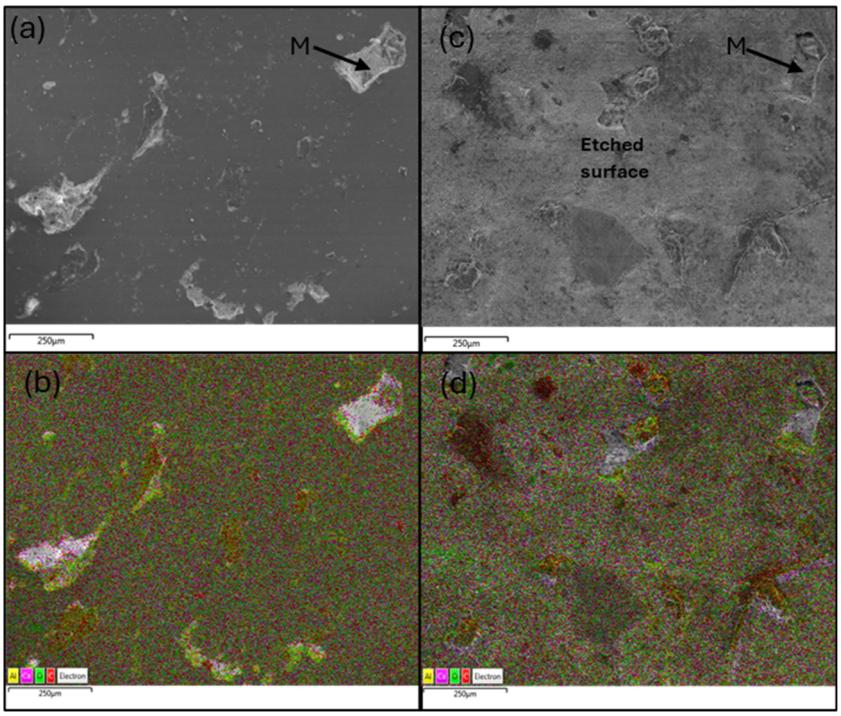

Fig. 7 SEM and EDS images of the surface of Indiana limestone before (a and b) and after (c and d) CO_2-water exposure. M is a common point on (a) and (c). The image in (c) is slightly rotated and can be moved about 15° clockwise to match the image in (a). (c) Shows a much more etched surface compared to (a).

of chemically driven weakening that depends strongly on mineralogical composition, pore structure, and initial mechanical properties. Across all lithologies, Young's modulus decreased after exposure, but the severity of this reduction varied significantly, demonstrating that the long-term geomechanical stability of rocks in CO_2-rich environments is

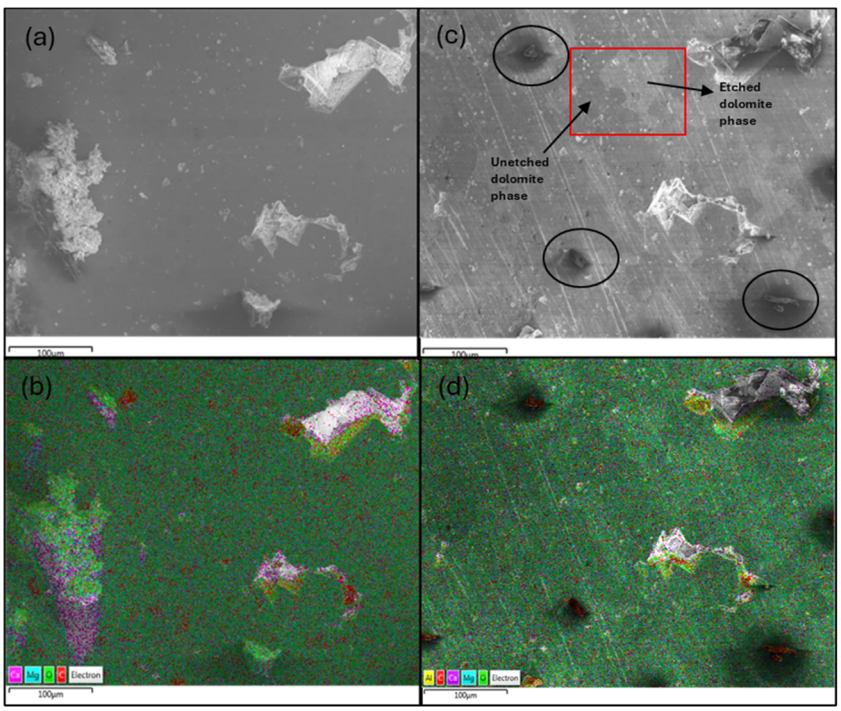

Fig. 8 SEM and EDS images of the surface of Silurian dolomite before (a and b) and after (c and d) CO_2-water exposure. The two likely dolomite phases appear in (c) with one showing more etched growth zones than the other. The circled areas on (c) are possible contaminants on the surface.

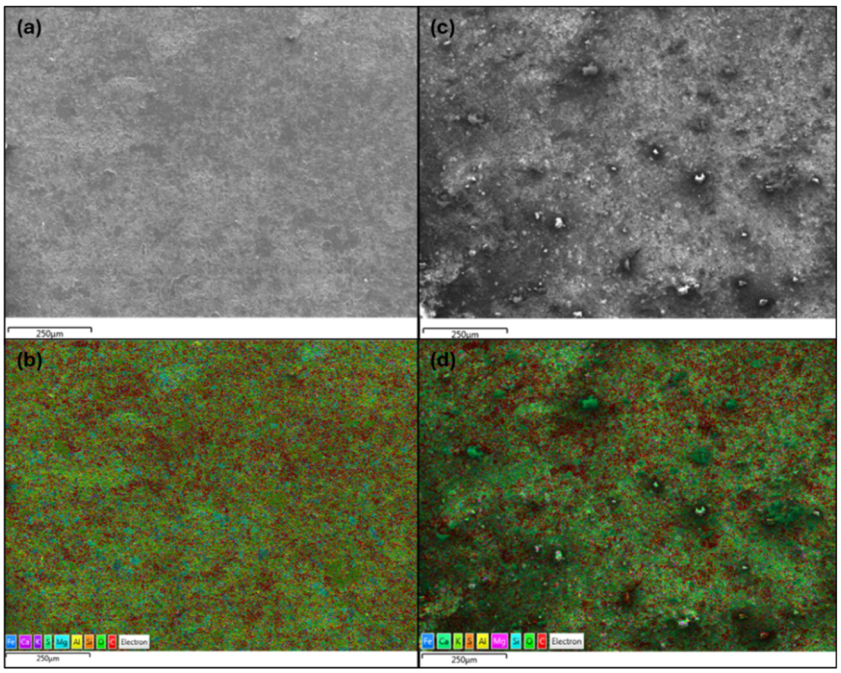

Fig. 9 SEM and EDS images of the surface of Woodford Shale before (a and b) and after (c and d) CO_2 exposure. Image (c) shows a possible damage to the surface with surface contamination.

inseparable from their mineralogical reactivity and microstructural evolution.

The geomechanical weakening observed across all rock types in this study is fundamentally controlled by chemical reactions occurring at the CO_2-water-rock interface. When CO_2 dissolves in water, it forms carbonic acid (H_2CO_3), which partially dissociates into bicarbonate (HCO_3^-) and hydrogen ions (H^+), lowering the pH of the system and promoting mineral dissolution reactions.[48,49] This acidification enhances the reactivity of minerals, particularly carbonate phases such as calcite and dolomite, which dissolve according to:

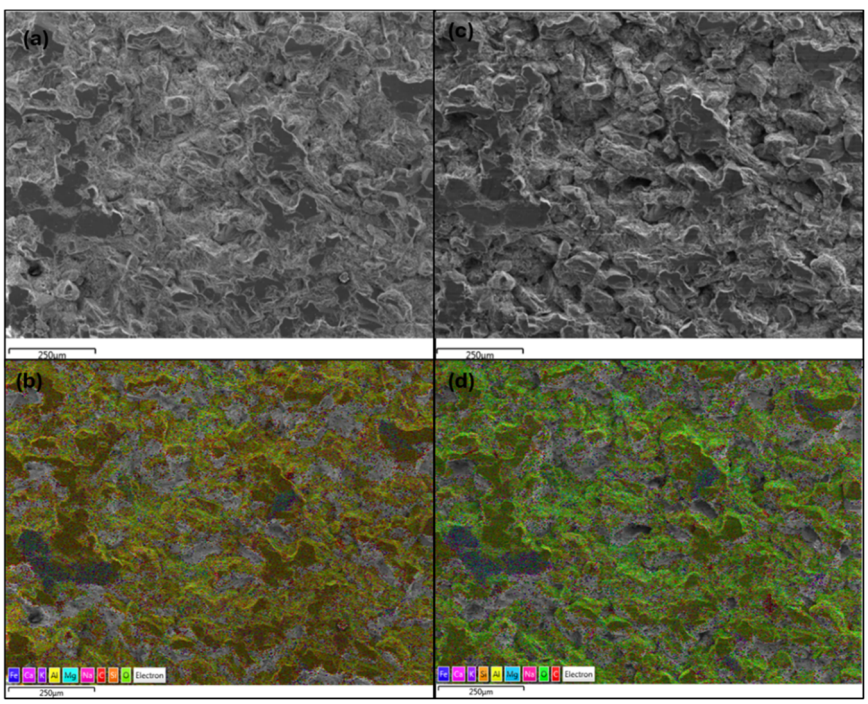

Fig. 10 SEM and EDS images of the surface of Bandera Sandstone before (a and b) and after (c and d) CO_2-water exposure. There were no clear observable alterations on the surface of (c).

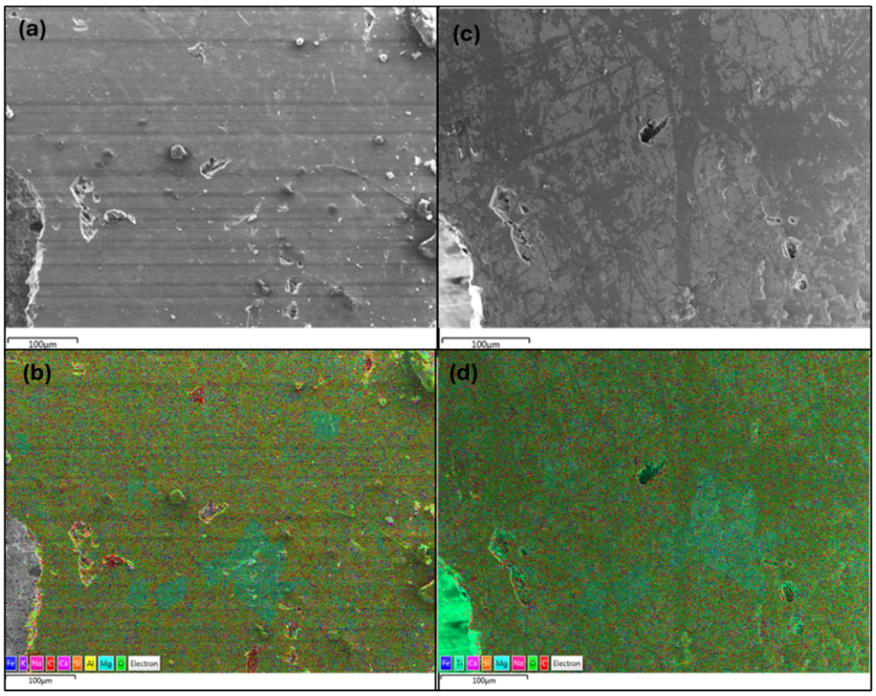

Fig. 11 SEM and EDS images of the surface of Iceland Basalt before (a and b) and after (c and d) CO_2-water exposure. The surface of (c) appears to have new crystallite growths in glass and also possibly some artifact from coating of the sample during SEM.

$$CaCO_3 + H^+ \rightarrow Ca^{2+} + HCO_3^-$$

The high Ca^{2+} concentrations measured in effluent solutions in this study directly confirm this dissolution mechanism and are consistent with previous experimental observations of CO_2-carbonate interactions.[1,27] The dissolution of load-bearing mineral phases reduces grain-to-grain contact and increases porosity, leading to a measurable reduction in Young's modulus. In silicate-rich rocks such as sandstone and basalt,

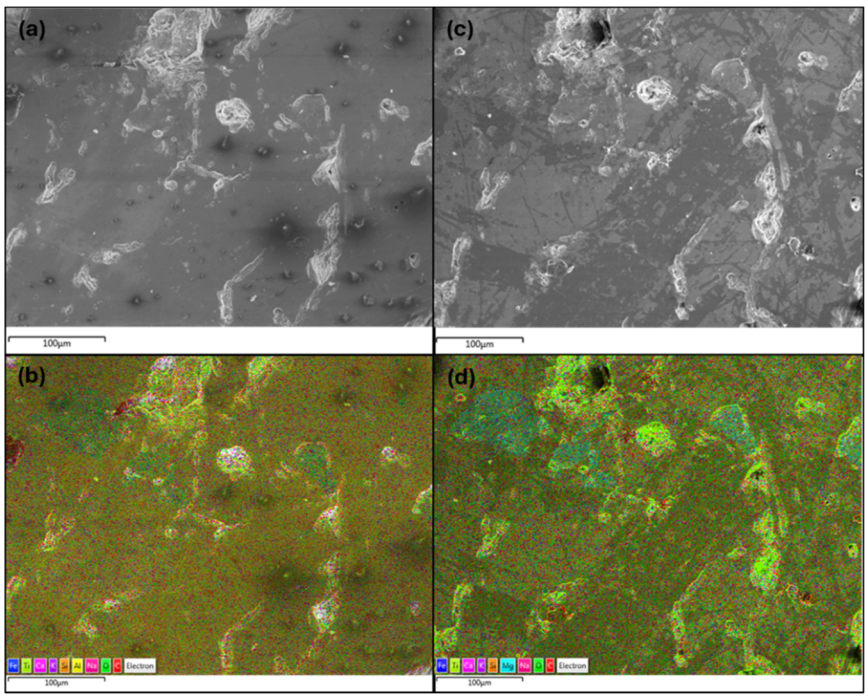

Fig. 12 SEM and EDS images of the surface of Carrizozo Basalt before (a and b) and after (c and d) CO_2-water exposure. The surface changes observed in (c) are possibly growth of crystallites in glass and some areas could also be artifacts from coating the surface for SEM analysis.

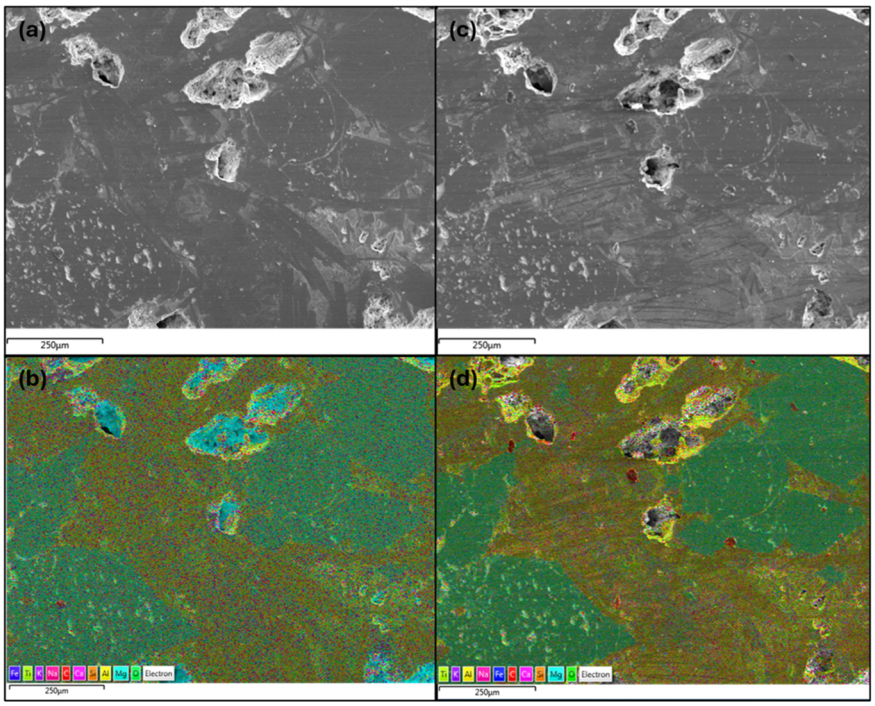

Fig. 13 SEM and EDS images of the surface of Kilbourne A before (a and b) and after (c and d) CO_2-water exposure. (C) Shows growth of crystallites in glass after reaction with CO_2. Some of the changes on surfaces could also be artifacts from handling the samples for coating during SEM.

dissolution reactions proceed more slowly due to the greater stability of silicate minerals. However, feldspars and mafic minerals (*e.g.*, pyroxenes, olivine) can undergo proton-promoted hydrolysis, releasing cations such as Na^+, Ca^{2+}, Mg^{2+}, and Fe^{2+} into solution.[50] The moderate concentrations of these ions observed in effluent analyses suggest ongoing but

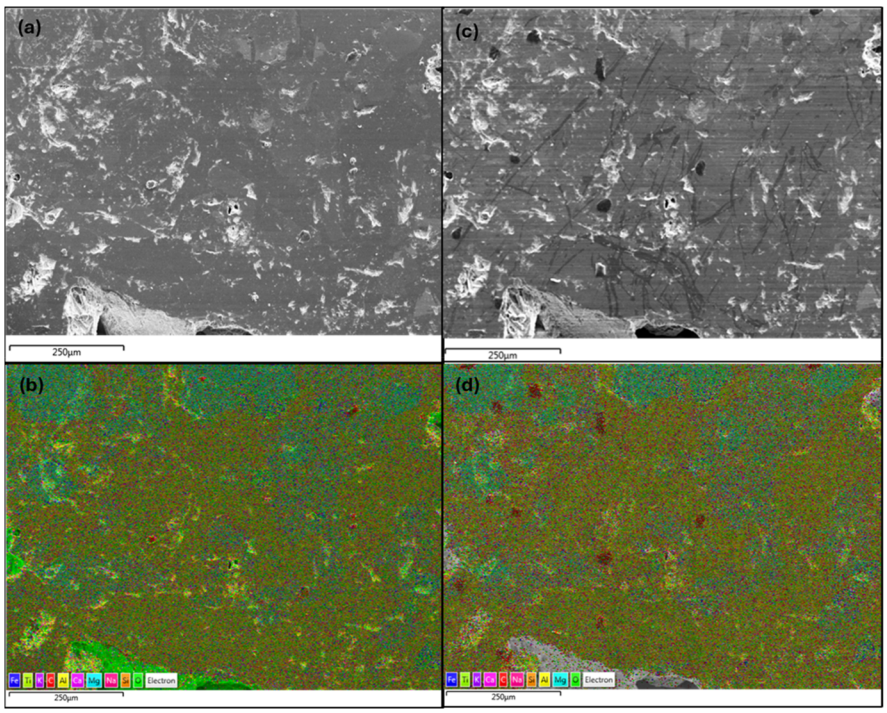

Fig. 14 SEM and EDS images of the surface of Kilbourne B before (a and b) and after (c and d) CO_2-water exposure. (C) Shows growth of crystallites in glass after reaction with CO_2. Some of the changes on surfaces could also be artifacts from handling the samples for coating during SEM.

Table 5 Summary of SEM-EDS observations before and after CO_2 exposure

Rock type	Pre-exposure features	Post-exposure changes	Elemental changes (EDS)
Woodford shale	Compact, flaky surface; low porosity	Minor etching; slight delamination	Slight decrease in Mg, Ca Al; increase in Al, S, Si, Fe
Indiana limestone	Smooth, interlocked crystals	Heavy dissolution; roughened surface; surface pitting	Decrease in Mg, Ca; increase in Si, Al
Bandera sandstone	Angular quartz grains; visible pores	Minor surface in filling	Generally stable Si; slight increase in Fe, Ti
Silurian dolomite	Crystalline, fine-grained surface	Very mild surface pitting; roughened texture, etching of a late growth stage of the dolomite but not an early one	Decrease in Ca, Mg, Al; slight increase in Si
Carrizozo Basalt	Vesicular; plagioclase-rich	Mild etching	Slight Fe, Mg loss
Iceland Basalt	Fine-textured; possibly glassy	Minimal visible change	Decrease in Al, Fe, Ca, Na; increase in Si
Kilbourne A basalt	Fine-textured	Minimal visible change	Drop in Si, Ca, Mg, Al; slight rise in Fe, Ti
Kilbourne Basalt B	Fine-textured	Minimal visible change	Drop in Na, Mg; rise in Si, ti

kinetically limited dissolution. In basalts, these reactions may also promote secondary carbonate precipitation, which can partially offset mechanical weakening by filling pore spaces over time.[25] In shale, the interaction is further complicated by ion exchange and clay-fluid interactions, where H^+ replaces interlayer cations (*e.g.*, Na^+, K^+), leading to swelling and structural weakening.[28] This process contributes to the reduction in stiffness observed despite limited visible dissolution in SEM images.

The extent and rate of CO_2-water-rock interactions are strongly influenced by the structure and speciation of CO_2 in the aqueous phase. Dissolved CO_2 exists in equilibrium between molecular CO_2(aq), carbonic acid (H_2CO_3), bicarbonate (HCO_3^-), and carbonate (CO_3^{2-}), with their relative abundances controlled by pressure, temperature, and pH.[49] At the experimental conditions used in this study (40 °C and 1200 psi), CO_2 solubility is elevated, resulting in increased formation of carbonic acid and enhanced proton availability, which drives mineral dissolution. At the molecular level, the hydration of CO_2 and formation of carbonic acid alter the hydrogen-bonding structure of water, influencing solvent properties such as dielectric constant and ion mobility.[51] These changes affect the transport of reactive species to mineral surfaces and the detachment of ions from crystal lattices. For example, increased proton activity enhances the breaking of metal–oxygen bonds in carbonate and silicate minerals, accelerating dissolution kinetics.[50] As dissolution progresses, the accumulation of aqueous ions modifies the fluid chemistry, potentially leading to supersaturation and secondary mineral precipitation, particularly carbonate phases in basaltic systems.[25] This dynamic interplay between dissolution and precipitation reflects a feedback mechanism between fluid structure and mineral stability.

Therefore, the observed geomechanical changes can be understood as the macroscopic expression of microscale chemical processes governed by aqueous speciation, fluid structure, and mineral reactivity.

A student's *t*-test at a 95% confidence level ($\alpha = 0.05$) was used to evaluate the reproducibility of mechanical changes observed following CO_2 exposure. Young's modulus decreased significantly in Dolomite ($p = 0.018$), Iceland Basalt ($p = 0.046$), Kilbourne Basalt A ($p = 0.043$), and Indiana Limestone ($p \approx 2.34 \times 10^{-7}$). These rocks not only revealed significant decreases in average stiffness, but also noticeable shifts in variability, as indicated by their standard deviations. Dolomite dropped from 148.38 GPa (±21.47) to 100.23 GPa (±4.87), with a significant decrease in standard deviation, indicating a more consistent weakening across samples. Indiana Limestone saw a significant decrease in modulus from 59.45 GPa (±2.34) to 6.11 GPa (±1.42), indicating severe interfacial mechanical degradation.

Iceland Basalt reduced its average modulus from 105.99 GPa (±34.39) to 53.07 GPa (±16.38). While there was a noticeable decrease in stiffness, the relatively high standard deviations before and after exposure indicate moderate sample variability. Kilbourne Basalt A's average modulus decreased dramatically from 27.74 GPa (±10.08) to 11.05 GPa (±1.89) after exposure, indicating a more consistent mechanical response. Standard deviation trends varied in rocks with no statistically significant change, such as Woodford Shale ($p = 0.063$), Sandstone ($p = 0.925$), Carrizozo Basalt ($p = 0.206$), and Kilbourne Basalt B ($p = 0.121$). Woodford Shale modulus decreased from 6.21 GPa (±1.78) to 3.70 GPa (±1.17), with less fluctuation, although the *p*-value was just above the significance level. Sandstone had nearly the same average modulus (21.65 GPa before *vs.* 20.63 GPa after), but the standard deviation increased significantly from ±1.74 to ±19.98, indicating highly inconsistent responses across samples, possibly due to heterogeneities in cementation or grain structure.

Variation among basalts. The modulus of Carrizozo Basalt decreased from 118.63 GPa (±42.74) to 82.86 GPa (±23.52). While there was some variability reduction, it was not statistically significant. Kilbourne Basalt B's drop from 69.53 GPa (±17.67) to 49.37 GPa (±17.67) remained consistent before and after exposure, leading to a nonsignificant finding.

Basalts' moderate to severe reductions in stiffness, with variability were most likely controlled by reactive mineral phases, glass content, and porosity. Carrizozo Basalt's mechanical reduction was likely due to the presence of more stable minerals such as quartz and diopside, which are less susceptible to dissolution in acidic fluids. In contrast, Iceland basalt's substantial and significant drop in modulus was consistent with its higher glass content and porosity, which enhanced fluid–rock interaction and promoted accelerated dissolution. Kilbourne Basalt A with the most severe basalt weakening, corresponds to the reactivity of augite and labradorite phases. SEM-EDS observations supported this behaviour, revealing significant etching of darker mineral patches and broad elemental loss, indicating active dissolution of highly reactive mafic minerals and potential glass content. Kilbourne Basalt B, despite its larger augite proportion, did not show statistically significant mechanical reduction ($p = 0.121$). Effluents from the Kilbourne A and B reactions revealed the release of a high concentration of Ca^{2+}, possibly from glass hinting at the susceptibility of these samples to CO_2 rich environments. SEM-EDS results similarly indicated limited surface alteration compared to Kilbourne A, suggesting that pore structure and degree of crystallinity may offset mineralogical reactivity. Altogether, the combined mechanical and surface analyses demonstrate that basalts with higher glass or mafic content are more susceptible to dissolution but may simultaneously promote mineral carbonation, whereas more crystalline basalts exhibit greater mechanical stability.

Limestone and dolomite. The severe mechanical degradation of carbonate rocks was due to the high solubility of carbonate minerals in CO_2-acidified water. With the largest reduction in stiffness in Indiana limestone, SEM-EDS images revealed extensive micropore development, crystal-edge dissolution, and increased surface roughness, fully consistent with calcite dissolution. Effluent analysis revealed that there was a substantial Ca^{2+} concentration, indicating that the highly reactive calcite mineral had clearly been dissolved. These changes significantly compromise limestone's integrity and demonstrate its vulnerability in CO_2-rich environments.

With Silurian dolomite, having also shown a significant stiffness loss, SEM-EDS revealed dissolution pits, variable Ca : Mg ratios, and evidence of two dolomite phases with differing reactivity, one that rapidly etched, and another that was more stable. Though dolomite is more resistant than calcite, these findings confirm that som dolomite compositions still undergo measurable structural and chemical weakening, with implications for reservoir stability. Collectively, carbonate dissolution increases porosity and permeability and may improve injectivity near the wellbore, but it also poses risks to long-term reservoir strength, especially as mineral dissolution may lead to compaction or reprecipitation farther from injection zones and near the producers in EOR projects.

Sandstone and shale. Quartz-rich sandstone's strong mechanical resilience, with Young's modulus decreasing only slightly and SEM-EDS results confirming its low reactivity is likely due to the presence of quartz. Small increases in Ca and Fe suggested limited secondary mineral precipitation, but no major textural changes occurred. These results indicate that sandstone maintains structural stability under CO_2-rich conditions, though long-term exposure could gradually influence cement phases and reduce permeability through localized pore clogging.

SEM-EDS in Woodford Shale showed limited visible dissolution but revealed film-like coatings with increases in surface composition of Al, Fe, and C, indicating subtle chemical alteration at the surface. Despite its chemical stability, the clay-rich composition (muscovite and zinnwaldite ~55%) means that CO_2-acidified water promotes softening, interlayer swelling, and reduction in cohesive strength.

With effluents from Woodford shale and Bandera sandstone having moderate quantities of Ca^{2+}, Na^{+}, and Mg^{2+}, indicating that they were vulnerable to the acidic environment. These ions are most likely released from the albite and dolomite mineral phases found in the sandstone and Woodford shale samples, respectively. For shale, this suggests potential deterioration of shale caprock sealing capacity over time, though increased ductility may mitigate brittle failure.

Comparative overview and implications

Mineralogy definitely plays a crucial role in controlling the interactions between CO_2, water, and rock. Carbonate rocks, such as limestone and dolomite, may show improved porosity and permeability due to dissolution, thereby improving injectivity for EOR and CO_2 sequestration.[52] However, there are concerns about long-term reservoir stability since rock softening may impact porosity and especially permeability, which are lowered by compaction. Furthermore, dissolved elements from the close injection point may precipitate in a different water composition environment further away from the injection point. Basalts show potential due to their capacity to produce mineral carbonation, particularly those rich in reactive mafic minerals; nevertheless, diversity between samples must be noted, since some display geomechanical stability while others do not. Though shale demonstrated chemical stability, its large decrease in stiffness does not support its use as an effective caprock for CO_2 storage.

In summary, SEM-EDS analysis shed light on the geochemical processes at the rock–fluid interface during CO_2 storage. Surface textures and elemental profiles clearly demonstrate variable degrees of dissolution, mineral transformation, and probable secondary mineral precipitation, all of which contribute to these rocks' capacity for long-term geologic carbon storage.

The statistical trends across rock types align with the mineralogical insights from SEM-EDS. Significant mechanical changes were associated with rocks showing strong dissolution features in Indiana limestone, dolomite, Iceland basalt, and Kilbourne A, all of which exhibited notable reductions in surface integrity and accompanying shifts in elemental composition. Rocks with nonsignificant statistical changes (Carrizozo Basalt, Kilbourne B, sandstone, shale) generally showed limited or uneven surface alteration, emphasizing the tight coupling between mineral reactivity and mechanical response.

Overall, the integrated mechanical and SEM-EDS results reinforce that mineralogy governs the extent of CO_2-induced weakening. Carbonate-rich rocks, especially limestone, undergo the most severe dissolution-driven degradation. Dolomite is more resilient but still vulnerable. Quartz-rich sandstones remain mechanically stable with minimal chemical alteration. Basalts show variable responses depending on glass content and mafic mineralogy: reactive basalts weaken substantially but hold potential for mineral carbonation, while more crystalline basalts maintain better mechanical integrity. Shales, though chemically stable, experience significant stiffness reduction due to clay–water interactions. These combined findings highlight the necessity of selecting CO_2 storage formations based not only on porosity and injectivity, but also on mineralogical stability and long-term geochemical behavior to ensure reservoir integrity in carbon storage applications.

Limitations and implications for long term CO_2 storage. While this study provides important insights into the geomechanical and geochemical effects of CO_2-water–rock interaction, several limitations must be acknowledged when interpreting the results in the context of long-term carbon storage applications. The experiments were conducted over a relatively short duration (5 days), whereas CO_2 storage in CCS and CCUS systems occurs over timescales ranging from decades to thousands of years. As such, the results primarily capture early-stage reaction kinetics and near-surface mineral alterations rather than long-term equilibrium behavior.

The selection of a 5-day exposure period was based on preliminary testing using Indiana limestone, where rapid dissolution-driven weakening stabilized between 96 and 120 hours. While this provides a reasonable benchmark for highly reactive carbonate systems, it may not fully represent slower-reacting lithologies such as basalts and quartz-rich sandstones, where reaction kinetics are significantly reduced. In such systems, mineral dissolution, secondary precipitation, and pore structure evolution may continue over much longer timescales.

Furthermore, the experiments were conducted under static conditions using small ($7 \times 7 \times 3$ mm) polished samples. These conditions represent static rather than dynamic measurements. In subsurface environments, continuous CO_2 injection and brine movement can significantly influence dissolution–precipitation dynamics, potentially leading to mineral trapping, pore clogging, or redistribution of dissolved species over larger spatial scales.

Additional long-term processes not captured in this study include cumulative clay swelling in shale formations, progressive mineral carbonation in basalts, and diagenetic alterations that may either enhance or reduce mechanical integrity over time. These coupled geochemical-geomechanical processes require extended-duration experiments and numerical modeling to fully understand their impact on reservoir performance.

Therefore, the findings of this study should be interpreted as providing grain-scale and short-term mechanistic insights into CO_2-induced weakening rather than direct predictions of long-term reservoir behavior.

Conclusions

This study evaluated how CO_2-water interactions affect the geomechanical properties of different rock types, namely Young's modulus. The study revealed that mineralogy is critical in influencing a rock's mechanical stability following exposure to CO_2-rich fluids. The results indicated mechanical weakening assessed by nanoindentation measured in proximity to the CO_2-water-rock interface, where the interaction was most prevalent. Carbonate rocks, notably Indiana Limestone, demonstrated the most severe reduction in stiffness (~90%) due to calcite dissolution, as seen by a decrease in calcium content at specified places. This highlights the great vulnerability of pure limestones to CO_2-induced weakening. In contrast, Silurian dolomite, while also affected by some dissolution in certain compositional growth phases, exhibited greater resilience, with a moderate 29% decrease in modulus, suggesting dolomite's lesser solubility than calcite. Young's modulus in basalts decreased significantly but to various degrees, with Carrizozo New Mexico Basalt losing 28% and Iceland Basalt losing over 50%. Kilbourne A and B basalts saw a reduction in modulus by 67% and 29% respectively. The Carrizozo sample's less reactive nature could be attributed to the presence of more stable mineral phases such as quartz and diopside. The reduction in Iceland Basalt implies that basalts with high glass content are more susceptible to chemical alteration under CO_2-rich circumstances, while plagioclase-dominated basalts maintain better structural integrity. This was not constant across all basalt samples, indicating that the plagioclase and pyroxene minerals in the samples had varied reactivity. Alternatively, the varying reactivity of the basalt samples could be due to their glass content. These findings demonstrate that, while typically strong, basalts may experience significant mechanical weakening depending on their unique mineral assemblages and porosity. Quartz-rich sandstone demonstrated minimal alteration (~7% reduction), demonstrating the durability of quartz-dominated rocks in CO_2 storage conditions. Sandstone formations are resilient due to the presence of durable quartz and low-calcium feldspar minerals, making them ideal sinks for CO_2 injection due to their mechanical integrity. In contrast, Woodford shale experienced a 41% decline in Young's modulus despite little geochemical change to the material. The reduction could be caused mostly by clay swelling, minor mineral dissolution, and microfracturing, indicating a potential loss of caprock sealing capacity over time. The conclusions of this study have important implications for EOR, geological carbon storage, reservoir integrity, and subsurface engineering. Both limestone and dolomite reservoirs may weaken owing to dissolution, although sandstone deposits may be more stable for CO_2 storage. Long-term exposure to CO_2-water interactions can weaken caprock integrity in shale formations, requiring extensive evaluation. Future study should include long-term exposure studies, field-scale validations, and geochemical-mechanical modeling to better anticipate rock behavior under prolonged CO_2 exposure.

These findings highlight the significance of conducting rock-specific geomechanical evaluations in CO_2 EOR and

sequestration projects. This should ensure that subsurface formations chosen for long-term CO_2 injection maintain structural stability, prevent leakage, and support large-scale initiatives to combat climate change.

Author contributions

William Holdbrook Dontoh: lab investigation; data curation; formal analysis; visualization writing – original draft; writing – review and editing. Robert Goldstein: methodology, validation; review and editing. Kim Mews: methodology, review. Syung Tsau: methodology, validation; review and editing. Mubarak Alhajeri: conceptualization, validation, review and editing. Reza Barati: conceptualization; methodology; investigation; validation; supervision; funding; acquisition; project administration; resources; writing – review and editing.

Conflicts of interest

There are no conflicts to declare.

Data availability

All experimental datasets generated and analysed in this study, including processed petrophysical measurements (*e.g.*, strength, porosity, elastic modulus), mineralogical characterisation files (SEM-EDS outputs, XRD scans), and CO_2-exposure test results, can be available upon request.

Acknowledgements

We greatly acknowledge the financial support from the Tertiary Oil Recovery Program (TORP) and the Kansas Interdisciplinary Consortium on Earth, Energy and Environment (KICE^3) at The University of Kansas for their support of this porject.

References

1 C. Noiriel, L. Luquot, B. Madé, L. Raimbault, P. Gouze and J. van der Lee, Changes in Reactive Surface Area during Limestone Dissolution: An Experimental and Modelling Study, *Chem. Geol.*, 2009, **265**(1), 160–170, DOI: 10.1016/j.chemgeo.2009.01.032.

2 Y. Zhang, L. Shi, Z. Ye, L. Chen, N. Yuan, Y. Chen and H. Yang, Experimental Investigation of Supercritical CO2–Rock–Water Interactions in a Tight Formation with the Pore Scale during CO2–EOR and Sequestration, *ACS Omega*, 2022, 7(31), 27291–27299, DOI: 10.1021/acsomega.2c02246.

3 A. P. Gysi and A. Stefánsson, Experiments and Geochemical Modeling of CO2 Sequestration during Hydrothermal Basalt Alteration, *Chem. Geol.*, 2012, **306–307**, 10–28, DOI: 10.1016/j.chemgeo.2012.02.016.

4 G. J. Stosur, J. R. Hite, N. F. Carnahan and K. Miller, *The Alphabet Soup of IOR, EOR and AOR: Effective Communication Requires a Definition of Terms*, 2003, p. SPE-84908-MS.

5 W. M. Mahmud, S. Elmabrouk and H. K. B. Mahmud, Investigating Relative Permeability Measurements Using Unsteady-State Core Flooding Method, *Int. J. Pet. Petrochem. Eng.*, 2017, **3**(4), 54–64, DOI: 10.20431/2454-7980.0304005.

6 D. F. Martin and J. J. Taber, Carbon Dioxide Flooding, *J. Pet. Technol.*, 1992, **44**(04), 396–400, DOI: 10.2118/23564-PA.

7 M. Shimokawara, E. Yogarajah, T. Nawa and S. Takahashi, Influence of Carbonated Water-Rock Interactions on Enhanced Oil Recovery in Carbonate Reservoirs: Experimental Investigation and Geochemical Modeling, *J. Jpn. Pet. Inst.*, 2019, **62**(1), 19–27, DOI: 10.1627/jpi.62.19.

8 X. Wang, X. Wang, W. Hu, Y. Wan, J. Cao, C. Lv, R. Wang and M. Cui, Supercritical CO2-Involved Water–Rock Interactions at 85°C and Partial Pressures of 10–20 MPa: Sequestration and Enhanced Oil Recovery, *Energy Explor. Exploit.*, 2017, **35**(2), 237–258, DOI: 10.1177/0144598716687933.

9 M. R. Okhovat, K. Hassani, B. Rostami and M. Khosravi, Experimental Studies of CO2-Brine-Rock Interaction Effects on Permeability Alteration during CO2-EOR, *J. Pet. Explor. Prod. Technol.*, 2020, **10**(6), 2293–2301, DOI: 10.1007/s13202-020-00883-8.

10 S. Liang, Review of the CO_2-Water-Rock Interaction in Reservoir, *Bull. Mineral. Geochem.*, 2011, 104–112.

11 A. Palmer, C. Hendriks, O. Kaarstad and M. Ozaki, *Summary Of The Ipcc Special Report On Carbon Dioxide Capture And Storage*, 2006, pp. 179–194.

12 B. Smit, Carbon Capture and Storage: Introductory Lecture, *Faraday Discuss.*, 2016, **192**, 9–25, DOI: 10.1039/c6fd00148c.

13 A. S. Ahmed, Md. R. Rahman and M. K. Bin Bakri, A Review Based on Low- and High-Stream Global Carbon Capture and Storage (CCS) Technology and Implementation Strategy, *J. Appl. Sci. Process Eng.*, 2021, **8**, 722–737, DOI: 10.33736/jaspe.3157.2021.

14 H. Herzog, *Carbon Dioxide Capture and Storage*, ed.Helm, D., Hepburn, C., Oxford University Press, 2009, pp 263–283, DOI: 10.1093/acprof:osobl/9780199573288.003.0013.

15 T. Wang, H. Wang, F. Zhang and T. Xu, Simulation of CO2–Water–Rock Interactions on Geologic CO2 Sequestration under Geological Conditions of China, *Mar. Pollut. Bull.*, 2013, **76**(1), 307–314, DOI: 10.1016/j.marpolbul.2013.08.014.

16 G. Yang, Y. Li, A. Atrens, Y. Yu and Y. Wang, Numerical Investigation into the Impact of CO2-Water-Rock Interactions on CO2 Injectivity at the Shenhua CCS Demonstration Project, China, *Geofluids*, 2017, **2017**(1), 4278621, DOI: 10.1155/2017/4278621.

17 J. Kaszuba, B. Yardley and M. Andreani, Experimental Perspectives of Mineral Dissolution and Precipitation Due to Carbon Dioxide-Water-Rock Interactions, *Rev. Mineral. Geochem.*, 2013, **77**(1), 153–188, DOI: 10.2138/rmg.2013.77.5.

18 Carrizozo Lava Flow | U.S. Geological Survey. https://www.usgs.gov/volcanoes/carrizozo-lava-flow (accessed 2025-06-16).

19 D. W. Peate, J. A. Baker, S. P. Jakobsson, T. E. Waight, A. J. R. Kent, N. V. Grassineau and A. C. Skovgaard, Historic Magmatism on the Reykjanes Peninsula, Iceland: A Snap-Shot of Melt Generation at a Ridge Segment,

Contrib. Mineral. Petrol., 2009, **157**(3), 359–382, DOI: 10.1007/s00410-008-0339-4.

20 E. W. Marshall, A. Caracciolo, E. Bali, S. A. Halldórsson, S. Matthews, E. Ranta, M. B. Rasmussen, J. G. Robin, G. H. Guðfinnson, J. Maclennan, C. Bosq, D. Auclair, O. Sigmarsson, H. Merrill, B. Gísladóttir, S. Johnson, N. Löw, A. Stracke and F. Genske, The Petrology and Geochemistry of the 2021 Fagradalsfjall Eruption, Iceland: An Eruption Sourced From Multiple, Compositionally Diverse, Near-Moho Sills, *AGU Adv.*, 2024, **5**(6), e2024AV001310, DOI: 10.1029/2024AV001310.

21 C. Noiriel, B. Madé and P. Gouze, Impact of Coating Development on the Hydraulic and Transport Properties in Argillaceous Limestone Fracture, *Water Resour. Res.*, 2007, **43**(9), WR005379, DOI: 10.1029/2006WR005379.

22 H. G. Machel, Concepts and Models of Dolomitization: A Critical Reappraisal, *Geol. Soc. Spec. Publ.*, 2004, **235**(1), 7–63, DOI: 10.1144/GSL.SP.2004.235.01.02.

23 J. M. Ajdukiewicz and R. H. Lander, Sandstone Reservoir Quality Prediction: The State of the Art, *AAPG Bull.*, 2010, **94**(8), 1083–1091, DOI: 10.1306/intro060110.

24 A Review on Shale Reservoirs as an Unconventional Play – The History, Technology Revolution, Importance to Oil and Gas Industry, and the Development Future - LIN - 2016 - Acta Geologica Sinica - English Edition - Wiley Online Library. https://onlinelibrary.wiley.com/doi/10.1111/1755-6724.12823?msockid=27bacb9b82c06fd50ce3df6b832e6e90 (accessed 2025-05-08).

25 J. M. Matter, M. Stute, S. Ó. Snæbjörnsdottir, E. H. Oelkers, S. R. Gislason, E. S. Aradottir, B. Sigfusson, I. Gunnarsson, H. Sigurdardottir, E. Gunnlaugsson, G. Axelsson, H. A. Alfredsson, D. Wolff-Boenisch, K. Mesfin, D. F. de la R. Taya, J. Hall, K. Dideriksen and W. S. Broecker, Rapid Carbon Mineralization for Permanent Disposal of Anthropogenic Carbon Dioxide Emissions, *Science*, 2016, **352**(6291), 1312–1314, DOI: 10.1126/science.aad8132.

26 K. Kim, V. Vilarrasa and R. Y. Makhnenko, CO2 Injection Effect on Geomechanical and Flow Properties of Calcite-Rich Reservoirs, *Fluids*, 2018, **3**(3), 66, DOI: 10.3390/fluids3030066.

27 J. P. Kaszuba, D. R. Janecky and M. G. Snow, Carbon Dioxide Reaction Processes in a Model Brine Aquifer at 200 °C and 200 Bars: Implications for Geologic Sequestration of Carbon, *Appl. Geochem.*, 2003, **18**(7), 1065–1080, DOI: 10.1016/S0883-2927(02)00239-1.

28 Q. Lyu, P. G. Ranjith, X. Long, Y. Kang and M. Huang, A Review of Shale Swelling by Water Adsorption, *J. Nat. Gas Sci. Eng.*, 2015, **27**, 1421–1431, DOI: 10.1016/j.jngse.2015.10.004.

29 D. N. Espinoza and J. C. Santamarina, CO2 Breakthrough—Caprock Sealing Efficiency and Integrity for Carbon Geological Storage, *Int. J. Greenh. Gas Control*, 2017, **66**, 218–229, DOI: 10.1016/j.ijggc.2017.09.019.

30 S. Zhao, L. Liu and N. Liu, Petrographic and Stable Isotopic Evidences of CO2-Induced Alterations in Sandstones in the Lishui Sag, East China Sea Basin, China, *Appl. Geochem.*, 2018, **90**, 115–128, DOI: 10.1016/j.apgeochem.2018.01.004.

31 W. C. Oliver and G. M. Pharr, An Improved Technique for Determining Hardness and Elastic Modulus Using Load and Displacement Sensing Indentation Experiments, *J. Mater. Res.*, 1992, **7**(6), 1564–1583, DOI: 10.1557/JMR.1992.1564.

32 C. P. Bobko, Assessing the Mechanical Microstructure of Shale by Nanoindentation : The Link between Mineral Composition and Mechanical Properties, Doctoral thesis, Massachusetts Institute of Technology, 2008, https://dspace.mit.edu/handle/1721.1/47731, accessed 2025-05-09.

33 W. Zhu, J. J. Hughes, N. Bicanic and C. J. Pearce, Nanoindentation Mapping of Mechanical Properties of Cement Paste and Natural Rocks, *Mater. Charact.*, 2007, **58**(11), 1189–1198, DOI: 10.1016/j.matchar.2007.05.018.

34 E. C. David, N. Brantut, L. N. Hansen and T. M. Mitchell, Absence of Stress-Induced Anisotropy During Brittle Deformation in Antigorite Serpentinite, *J. Geophys. Res. Solid Earth*, 2018, **123**(12), 616–644, DOI: 10.1029/2018JB016255.

35 K. S. Mews, Application of Nano-Scale Geomechanics Using PeakForce Quantitative Nano-Mechanical Mapping to Improve Hydraulic Fracture Design in Highly Heterogeneous Reservoirs, MSc thesis, University of Kansas, 2020.

36 J. Němeček, Nanoindentation Based Analysis of Heterogeneous Structural Materials, in *Nanoindentation in Materials Science*, IntechOpen, 2012. DOI: 10.5772/50968.

37 N. K. Mukhopadhyay and P. Paufler, Micro- and Nanoindentation Techniques for Mechanical Characterisation of Materials, *Int. Mater. Rev.*, 2006, **51**(4), 209–245, DOI: 10.1179/174328006X102475.

38 G. Mavko; T. Mukerji and J. Dvorkin, *The Rock Physics Handbook: Tools for Seismic Analysis of Porous Media*, Cambridge university press, Cambridge, UK, 2nd edn, 2009.

39 P. Baud, A. Schubnel and T. Wong, Dilatancy, Compaction, and Failure Mode in Solnhofen Limestone, *J. Geophys. Res. Solid Earth*, 2000, **105**(B8), 19289–19303, DOI: 10.1029/2000JB900133.

40 P. M. Doyen, Permeability, Conductivity, and Pore Geometry of Sandstone, *J. Geophys. Res. Solid Earth*, 1988, **93**(B7), 7729–7740, DOI: 10.1029/JB093iB07p07729.

41 H. F. Wang, *Theory of Linear Poroelasticity with Applications to Geomechanics and Hydrogeology*; Princeton University Press, 2017, DOI: 10.1515/9781400885688.

42 A. S. Serasa, A. G. Rafek, W. S. W. Harun, M. Abdurrahman, L. K. Ern, N. X. Huy, T. V. Xuan, R. Roslee, M. Zhang and G. T. Lai, Correlation of Dynamic and Static Young's Modulus for Limestone, *IOP Conf. Ser.: Earth Environ. Sci.*, 2022, **1103**, 012032, DOI: 10.1088/1755-1315/1103/1/012032.

43 V. Mikhaltsevitch; M. Lebedev; B. Gurevich Laboratory Measurements of the Elastic and Anelastic Parameters of Limestone at Seismic Frequencies. In *SEG Technical Program Expanded Abstracts 2013*, SEG Technical Program Expanded Abstracts; Society of Exploration Geophysicists, 2013, pp 2974–2978, DOI: 10.1190/segam2013-1395.1.

44 Mechanical Properties of Natural Building Stone. doczz.net. https://doczz.net/doc/7453293/mechanical-properties-of-natural-building-stone (accessed 2025-05-14).
45 W. H. Dontoh; K. Mews; B. Ghanbarian; M. Alhajeri; R. Barati Measuring Variations in Rock Mechanical Properties Due to CO2 Injection: Application of Nano-Indentation.
46 S. Hangx, A. Van Der Linden, F. Marcelis and A. Bauer, The Effect of CO2 on the Mechanical Properties of the Captain Sandstone: Geological Storage of CO2 at the Goldeneye Field (UK), *Int. J. Greenh. Gas Control*, 2013, **19**, 609–619, DOI: 10.1016/j.ijggc.2012.12.016.
47 J. Li, S. Lu, H. Xue, L. Xie and P. Zhang, Quantitative Evaluation on the Elastic Property of Oil-Bearing Mudstone/Shale from a Chinese Continental Basin, *Energy Explor. Exploit.*, 2015, **33**(6), 851–868, DOI: 10.1260/0144-5987.33.6.851.
48 The Geochemistry of Natural Waters | The Groundwater Project. Httpsgw-Proj.
49 Geochemistry, Groundwater and Pollution Appelo and D - Postma, Second Edition 1 50 | PDF | Solubility | Redox. Scribd. https://www.scribd.com/document/459059791/Geochemistry-Groundwater-and-Pollution-Appelo-and-D-Postma-Second-Edition-1-50 (accessed 2026-04-07).
50 S. R. Gislason and E. H. Oelkers, Mechanism, Rates, and Consequences of Basaltic Glass Dissolution: II. An Experimental Study of the Dissolution Rates of Basaltic Glass as a Function of pH and Temperature, *Geochim. Cosmochim. Acta*, 2003, **67**(20), 3817–3832, DOI: 10.1016/S0016-7037(03)00176-5.
51 G. Sposito, *The Chemistry of Soils*, Oxford university press, New York, 2nd edn, 2008.
52 P. Longe, S. Molomjav, J.-S. Tsau, S. Musgrove, J. Villalobos, J. D'Erasmo, M. M. Alhajeri and R. Barati, Techno-Economic Evaluation of CO2-EOR and Carbon Storage in a Shallow Incised Fluvial Reservoir Using Captured-CO2 from an Ethanol Plant, *Geoenergy Sci. Eng.*, 2025, **246**, 213559, DOI: 10.1016/j.geoen.2024.213559.